



ELSEVIER

Available online at www.sciencedirect.com

SCIENCE @ DIRECT®

Advances in Space Research xxx (2005) xxx–xxx

**ADVANCES IN  
SPACE  
RESEARCH**  
(a COSPAR publication)

www.elsevier.com/locate/asr

## Laboratory simulation of magnetospheric plasma shocks

W. Horton<sup>a,\*</sup>, C. Chiu<sup>a</sup>, T. Ditmire<sup>a</sup>, P. Valanju<sup>a</sup>, R. Presura<sup>b</sup>, V.V. Ivanov<sup>b</sup>,  
Y. Sentoku<sup>b</sup>, V.I. Sotnikov<sup>b</sup>, A. Esaulov<sup>b</sup>, N. Le Galloudec<sup>b</sup>, T.E. Cowan<sup>b</sup>, I. Dexas<sup>c</sup>

<sup>a</sup> Institute for Fusion Studies, The University of Texas, 1 University Station C1500, Austin, TX 78712, USA

<sup>b</sup> Nevada Terawatt Facility, University of Nevada, Reno, NV 89506, USA

<sup>c</sup> University of Colorado, Boulder, CO, USA

Received 5 October 2004; received in revised form 1 December 2004; accepted 11 January 2005

### 10 Abstract

11 Laboratory experiments using a plasma wind generated by laser-target interaction are developed to investigate the creation of a  
12 shock in front of the magnetosphere and the dynamo mechanism. Magnetic obstacles are placed in the plasma wind and measure-  
13 ments of the electro density gradients surrounding the obstacles are recorded. The experiments are analyzed with the methods used  
14 in theoretical simulation of the solar-wind-driven magnetosphere interactions. The proposed experiments are thought to be relevant  
15 to understanding the electron acceleration mechanisms at work in shock-driven magnetic dipole confined plasma surrounding com-  
16 pact magnetized stars and planets. Electron shock acceleration mechanisms are discussed in some detail.  
17 © 2005 COSPAR. Published by Elsevier Ltd. All rights reserved.

18 *Keywords:* Magnetospheres; Bow shocks; Compact magnetized stars; Laser blow-off plasmas

### 20 1. Magnetospheres and bow shocks

21 Magnetospheres are ubiquitous in space and astro-  
22 physics, being formed from plasma winds streaming past  
23 magnetic planets and stars. In the solar system, we know  
24 a great deal about magnetospheres formed by the solar  
25 plasma wind interaction with Earth (Fälthammar,  
26 1973) and Jupiter (Dessler, 1983). We will use this  
27 knowledge in designing the laboratory astrophysical  
28 experiments. The scaling factor from the laboratory to  
29 the geophysical space scale is of order  $10^9$ . The scaling  
30 factor from the laboratory to a magnetic white dwarf  
31 is  $10^{12}$ .

32 Detailed parameters have been given in Horton and  
33 Chiu (2004) for the laser Z-pinch simulation of the  
34 Earth's bowshock. Here, we report some first results of  
35 the laser Z-pinch experiment performed at the Univer-

sity of Nevada. The Z-pinch produces magnetic field  
 $B \approx 8 \text{ T} = 8 \times 10^4 \text{ G}$  on the high-field side of the shock  
with a plasma density increase from  $10^{17}$  to  $10^{18} \text{ cm}^{-3}$   
across the shock front. The Mach number is  $M_s = 3$ .  
The astrophysical magnetosphere that is more  
approachable for laboratory simulations is that inferred  
to precede the Type Ia supernova. The Type Ia super-  
nova is modeled as the culmination of a plasma wind  
accreting on a white dwarf. White dwarfs (WD) typi-  
cally contain a strong magnetic field  $B \sim 10^8 \text{ G}$  pro-  
duced by the magnetic flux conserving collapse of stars  
with typical stellar magnetic fields  $B \sim 100 \text{ G}$ .

Pulsars provide much strong magnetic fields  
 $B \sim 10^8 \text{ T} = 10^{12} \text{ G}$ . It is difficult to model due to the  
large magnitude field as well as the key role played by  
the rotation speed. Some rotational effects may eventu-  
ally be modeled in the laboratory by using spherical di-  
poles with sufficient electric charge  $Q$  to reach the  
desired rotation frequency from  $v_\phi = r\omega = E_r/B =$   
 $-(Q/M_{dp})r$ .

\* Corresponding author.

E-mail address: horton@physics.utexas.edu (W. Horton).

We have developed the details of the simulation of the Earth's magnetosphere as a magnetic obstacle in the plasma wind emitted from the sun, which forms a plasma-electrodynamic dynamo that accelerates charged particles (Horton and Chiu, 2004). Because the plasma wind is supersonic, the stationary magnetic dipole can be viewed as a piston that drives a shock in the rest frame of the inflowing plasma (Zel'dovich and Raizer, 1966). The electron acceleration mechanisms are not well understood (for example, see Li et al. (1998), Li (2002), Sarris et al. (2002), compared with Summers et al. (1998, 2002), Summers and Thorne (2003) for two different theoretical models). For the Earth's magnetosphere, several different types of theories are used to model the production of the 30 keV–1 MeV electron fluxes measured by instruments on spacecraft in the Earth's magnetosphere. The same type of electron acceleration phenomenon is also found in the magnetosphere of Jupiter, and similar processes probably account for the electron energy fluxes inferred from synchrotron radiation from magnetic stars (Shapiro and Teukolsky, 1983; Tajima and Shibata, 2002).

Laser blow-off plasmas (London and Rosen, 1986) and laser-plasma diagnostics indicate that the plasma wind pressure should exceed  $P \sim 10^6$  Pa  $\sim 10$  atm for the laboratory simulation experiment. Thus, the dipoles need to have magnetic fields above 10 T to stand off the plasma wind. In this work, we propose to carry out modern, high magnetic field, laser-blow off experiments in the laboratory. We analyze the possibility of using high powered lasers target experiments to investigate the nature of interaction of the dipole with the plasma wind with laser blow-off plasmas from plastic foils. Both front side and back side plasmas ejecta are candidates for different types of plasma winds. The super strong magnetic dipoles are produced by the Zebra-pinch facility at the University of Nevada. Key objectives in the experiment are to create a shock from a magnetic obstacle, to create the dynamo electric field, and to measure electron energies.

### 1.1. Bow shocks from plasma winds on magnetic stars and planets

Mildly supersonic  $M_s = u/c_s \sim 1.4$ –5 plasma winds are common place in astrophysics and space physics. The winds may be associated with accretion onto a central star. Winds occur in the precursor phase to the Type Ia supernova (SNIa) where plasma is pulled into the magnetic white dwarf (WD) from the companion star. Plasma winds are intercepted by neutron stars (NS). After stars are ignited, the stellar wind outflow creates bow shocks at the magnetic planets and at the termination of the stellar outflow where the thermal pressure jumps to match that of the interstellar gas.

Due to the long history of magnetospheric spacecrafts with bow shock passages, we know a great deal about the microscale structure of collisionless bow shocks. This well-developed field has taken another large step forward with the detailed correlation measurements with the extensive instruments on the Four-Cluster spacecrafts (Escoubet et al., 2004). Clusters is a European space agency mission in operation for three years and planned to continue until December 2005. The inner spacecraft distances has been 600, 2000, 100 and 5000 km. The bow shock (Stasiewicz et al., 2003) is now clearly seen to consist of hundreds to thousands of microshocks that have widths of order of the ion skin depth  $\delta_i = c/\omega_{pi}$  which is comparable to the ion gyroradius  $\rho_i = v_i/\omega_{ci}$  for the solar wind plasma which has  $\beta_i = p_i/(B^2/2\mu_0)$  of order unity. The compression ratios of the magnetic field in the microshocks is observed to  $B/B_0 \sim \rho/\rho_0 \sim 2$ –7. Now, we discuss how the microshock is formed from the Hall-MHD description of the plasma.

The shock structure is propagating upwind with speed 250 km/s with respect to the plasma which is flowing toward the planetary dipole with speed 400 km/s. The magnetic field  $\theta$  is at about  $30^\circ$  to the flow velocity. This bulk plasma flow speed is 5.7 times the sound speed (70 km/s) and 13 times the Alfvén velocity (30 km/s). The pulses shapes are well resolved by the four spacecrafts and there are hundreds of these nonlinear pulses in the overall bow shock region. This shocked plasma streams around the magnetopause. The shocked plasma outside the magnetosphere is called the magnetosheath. The entry of plasma across the magnetopause into the magnetosphere proper is largely from a back flow from the down stream side of the planetary dipole. The spiky, nonlinear nature of the plasma in the bow shock was known earlier and named SLAMS for short large-amplitude magnetic structures. There are a variety of shapes to SLAMS some with little density variation and some with density depletions.

### 1.2. Hall-MHD microshock structures

We take  $\hat{x}$  to point upwind into the undisturbed plasma and  $\hat{z}$  (north) in the direction of the ambient normal magnetic field  $B_z(x)$ . We allow a  $B_x$  and there is a Hall current sheet  $j_y(x)$  in the shock front. The plasma wind of density  $n_w$  and electron temperature  $T_w$  flows with speed  $u$  with respect to the dipole  $M = B_s R_s^3$  where  $s$  denotes the surface of the dipole. The ion temperature is typically lower than the electron temperature so that the acoustic waves are given by  $\omega/k_x = c_s = (T_e/m_i)^{1/2}$  and the Mach number  $M_s = u/c_s > 1$ . Here, we restrict attention to the regime of  $M_s = 1$ –5 and take  $T_e \approx 5$ –10 eV. The plasma wind density will vary from  $n_e \sim 10$  cm $^{-3}$  for the Earth's magnetosphere to  $n_e \sim 10^{-3}$ – $10^{-2}$  cm $^{-3}$  for the interstellar winds and the

164 winds on to the compact stars (WD and NS). We post-  
165 pone the study of strong shocks  $M_s \gg 1$  to a later work.

166 The magnetic dipole obstacle in the plasma wind  
167 turns the positive ions and negative electrons in opposite  
168 directions creating the current layer  $j_y$  in the shock front  
169 which we take centered at  $x = 0$  in the frame moving  
170 with the shock. Clearly, the electrons are turned  
171 promptly over the short distance  $\rho_e = v_e/\omega_{ce}$  while the  
172 ions penetrate much deeper over the scale  $\rho_i = v_i/\omega_{ci}$   
173  $> 43\rho_e$ . This charge separation creates an electric  
174 field  $E_x$  pointing upwind that draws the electrons into  
175 the shock front for repeated attempts to pass through  
176 the shock front. The magnitude of the electric potential  
177 is  $\Delta\Phi = -\int^x E_x dx = B_0 B_z / (\mu_0 n_i e)$  as determined by the  
178 Hall-MHD description with massless electrons and  
179 charge quasi-neutrality. Here,  $B_0$  is the field upstream  
180 and  $B_z > B_0$  is the field in the shock front.

181 The shock structure is described as Hall physics since  
182 the ion and electron have opposite velocities in the shock  
183 front that differs strongly from the  $\mathbf{E} \times \mathbf{B}$  drift velocity.  
184 Thus, the Ohm's law is given by the electron momentum  
185 balance equation

$$187 \quad \mathbf{E} + \mathbf{u}_e \times \mathbf{B} = \mathbf{E} + \mathbf{u} \times \mathbf{B} - \frac{\mathbf{j} \times \mathbf{B}}{en_e} = \eta \mathbf{j}, \quad (1)$$

188 where  $\eta$  is the microscale resistivity produced by wave-  
189 particle scattering.

190 The ion velocity  $\mathbf{u}$  fluid is given by the ion momentum  
191 balance equation

$$193 \quad \frac{d\mathbf{u}}{dt} = \frac{e_i}{m_i} (\mathbf{E} + \mathbf{u} \times \mathbf{B}) + \mu \nabla^2 \mathbf{u} = \frac{1}{m_i n_i} \mathbf{j} \times \mathbf{B} + \mu \nabla^2 \mathbf{u}, \quad (2)$$

194 where the term is  $|en_j/m_i| \ll |j \times B/m_i n_i|$  omitted. The ion  
195 pressure gradient is also small for these shocks. The con-  
196 servation of mass is

$$198 \quad \frac{d\rho}{dt} = -\rho \nabla \cdot \mathbf{u} \quad (3)$$

199 and the equation of state is taken as cold ions with neg-  
200 ligible  $T_i/T_e$  and isothermal electrons  $T_e = \text{constant}$ .

201 Here, we summarize the Hall MHD shock compres-  
202 sional model. The shape of the pulse is determined by  
203 the ion viscosity  $\mu$ . The speed and compression ratio  
204 are determined by the Rankine-Hugoniot conditions  
205 for an oblique magnetic shock.

206 For a compressional disturbance propagating toward  
207 the Earth at speed  $u$  into undisturbed near-Earth plasma  
208 with  $v_x = 0$ ,  $\rho_0$ ,  $p_0$ ,  $B_{z0}$  fields, the Rankine-Hugoniot  
209 conditions are:

$$212 \quad \rho(u - v_x) = \rho_0 u, \quad (4)$$

$$215 \quad \rho v_x (v_x - u) + p_0 \left( \frac{u}{u - v_x} \right)^2 + \frac{B_{z0}^2}{2\mu_0} \left( \frac{u}{u - v_x} \right)^2 - \mu \frac{dv_x}{dx} = p_0 + \frac{B_{z0}^2}{2\mu_0}, \quad (5)$$

where we use Eq. (4) and the equations of state  $p = p_0(\rho/\rho_0)^2$  and  $B_z/\rho = \text{constant}$  rather than integrating the thermal balance equation. Here,  $\mu$  is the viscosity and we can use  $\rho(u - v_x) = \rho_0 u$  again in terms of Eq. (5).

Without viscosity, there are solitary wave pulses of space scale  $\delta_i = c/\omega_{pi}$  for the SLAMS (Stasiewicz et al., 2003). We have the fixed points ( $dv_x/dx = 0$ ) of Eq. (5) for the two solutions in front and behind the dipolarization pulses given by the roots of

$$222 \quad \mu \frac{dv_x}{dx} = -\rho_0 u v_x + \left( p_0 + \frac{B_{z0}^2}{2\mu_0} \right) \left[ \left( \frac{u}{u - v_x} \right)^2 - 1 \right] = 0$$

224 for  $0 < v_{x1} < u$ . (6) 227

For strong compressions, the down-tail Earthward flow speed is close to  $u$ . Thus, the fixed point ( $dv_x/dx = 0$ ) is at

$$232 \quad v_{x1} = u \left[ 1 - \left( \frac{p_0 + B_{z0}^2/2\mu_0}{u^2 \rho_0} \right)^{1/2} \right]. \quad (7)$$

The quadrature from Eq. (6) gives the shock speed profile and width  $D$  determined by the microscopic viscosity  $\mu$ . The compressional pulse shape is  $v_x(x) = v_{x1}/[1 + \exp(\rho_0 u(x - x_0)/\mu)]$  which goes to zero for  $x = \rho_0 u(x - x_0)/\mu \gg 1$  and goes to  $v_{x1}$  in the geotail for  $x \rightarrow -\infty$ . For Bohm-like viscosity  $D = \mu/(\rho_0 u) \sim c/\omega_{pi}$  to  $\rho_i$ .

## 2. First results of the bow shock simulations with laser blow-off plasma 240 241

The laboratory experiment allows for a scaled simulation of Geo-space and Astro-space phenomena. It is useful for understanding the basic physics and inferring models for the real systems, as well as for verifying existing models and simulation codes. In the initial experiments presented here, we characterize the three dimensional structure of the plasma interaction with the magnetic obstacle. Experimental results are obtained with time-resolved laser interferometry, schlieren imaging, and magnetic probes. The study reveals details of the dynamics of the transition region between the high dynamic plasma pressure region and the high magnetic pressure piston surrounding the current carrying rod shown in Fig. 1.

The expanding plasma is created by laser ablation of a solid plastic target, and the ambient magnetic field is generated by a linear current ( $B_\phi(r) \sim \mu_0 I/2\pi r$ ). The plasma flow is created by the "Tomcat" laser with pulse energy up to 5 J at 1  $\mu\text{m}$  wavelength and 6 ns pulse width. At best focus, the laser irradiance on target is higher than  $10^{13} \text{ W/cm}^2$ . The laser target is placed at  $x_0 = 8.5 \text{ mm}$  from the rod surface. The radius of the rod is 7 mm. So the target is  $d_0 = 15.5 \text{ mm}$  from the axis

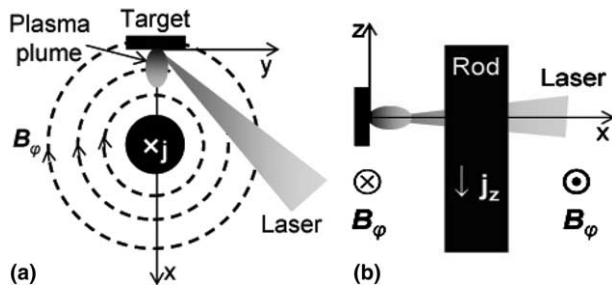


Fig. 1. Experimental set-up indicating the geometry of the magnetic field, laser illumination, and plasma expansion.

265 of the rod. The azimuthal magnetic field is produced by  
 266 axial current flowing in a rod acting as Z-pinch load in  
 267 the “Zebra” pulsed power generator used in a pulse re-  
 268 gime with maximum current 0.6 mA and rise time  
 269 200 ns. The laser is typically synchronized with the Z-  
 270 pinch such that the ablation plasma is produced and  
 271 evolves during a constant magnetic field period of about  
 272 30 ns at the current peak. The magnetic field strength in  
 273 vacuum is measured with magnetic probes.

274 To study the acceleration mechanism, the collisions  
 275 with neutrals or ions, that would knock electrons out  
 276 from the trapped state, have to be avoided. This puts  
 277 an upper limit on the collision frequency electron-neu-  
 278 tral or electron-ion (if the plasma radiation ionizes the  
 279 residual gas in the experiment chamber), as shown in  
 280 Horton (2004). The background pressure is maintained  
 281 lower than 10  $\mu$ Torr to maintain a negligible collision  
 282 frequency in the ambient plasma. For the current pulse  
 283 used, the surface temperature of the 7 mm radius rod in-  
 284 creases with less than 100 K above room temperature, so  
 285 no contaminant desorption or plasma formation from  
 286 the rod are expected. Assuming desorption takes place,  
 287 to expand 5 mm in 200 ns a hydrogen plasma would re-  
 288 quire that surface temperature of the rod to rise beyond  
 289  $T = 1$  eV ( $\sim 10^4$  K), which is unlikely.

290 In Fig. 2 two time snapshots from the schlieren diag-  
 291 nostic system that measures the electron density gradi-  
 292 ents are shown. The shock front has the steepest  
 293 gradient and shows up as the hemispherical surfaces in  
 294 both the  $x$ - $y$  plane perpendicular to the rod and in the  
 295  $x$ - $z$  plane perpendicular to the magnetic field. An addi-  
 296 tional short laser pulse is used to create the two-frame  
 297 interferometry images. The delay between frames was  
 298 7 ns. The overall space resolution was better than  
 299 25  $\mu$ m for schlieren imaging and about 100  $\mu$ m for  
 300 interferometry.

301 A plasma front with steep density gradient develops  
 302 at about 3 ns after the beginning of the laser pulse. Most  
 303 likely it consists of hydrogen ions that expand faster  
 304 than fully ionized carbon ions. The hydrogen plasma  
 305 front is sufficiently conductive so that the magnetic field  
 306 exclusion from the volume behind the front is almost  
 307 complete. While the front is slowed down by the interac-

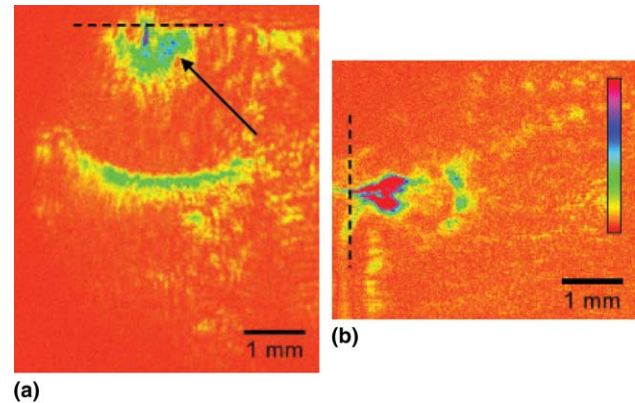


Fig. 2. Schlieren snapshots recorded from two experiments at 5 (a) and 4 ns (b) after the beginning of the heating laser pulse. Image (a) is recorded in the plane perpendicular to the rod (illustrated in Fig. 1(a)). The arrow indicates the direction of the laser beam. Image (b) is recorded in the plane perpendicular to the field (see Fig. 1(b)). In both images the dashed line indicates the target position. The laser beam is incident on the target as indicated in Fig. 1.

tion with the external magnetic field, the plasma from its  
 308 interior expands freely. Eventually this plasma compo-  
 309 nent, which is richer in carbon catches up and mixes  
 310 with the front plasma. Being more energetic, the carbon  
 311 component affects greatly the dynamics and parameters  
 312 of the plasma-field interface. Schlieren and interferome-  
 313 try show that eventually the plasma concentrates in a  
 314 plasma shell with thickness and gradient size scale ( $1/$   
 315  $L_n = \nabla n/n$ )  $L_n \approx 0.3$ – $0.5$  mm. According to PIC simu-  
 316 lations, although, the species separation is important at  
 317 the beginning of the plasma expansion, the plasma shell  
 318 becomes homogeneous due to the interaction with the  
 319 magnetic field.

320 The laser beam causes ablation of the target material,  
 321 releasing energetic ions of carbon and hydrogen.

322 The cloud of ablated plasma expands with the veloci-  
 323 ty  $v_{ex} \approx 3c_s$ , where  $c_s = \sqrt{(\gamma Z)_{eff} T / m_{eff}}$  is the speed of  
 324 sound. The effective quantities are defined by the equa-  
 325 tions  $(\gamma Z)_{eff} = \gamma_e(Z_C + NZ_H) + (1 + N)\gamma_i$  and  $m_{eff} =$   
 326  $(A_C + NA_H)m_p$ , and  $T$  is the temperature of each species  
 327 (electrons, protons, and carbon ions). The adiabatic  
 328 constants for electrons and ions are  $\gamma_e = 1$  and  $\gamma_i = 5/3$ ,  
 329 respectively, both ion species, carbon and hydrogen,  
 330 are considered fully ionized ( $Z_C = 6$ ,  $Z_H = 1$ , respec-  
 331 tively),  $A_C$  and  $A_H$  are the atomic masses of carbon  
 332 and hydrogen, respectively,  $N = 2$  is the hydrogen-to-  
 333 carbon ratio ion density,  $m_p$  is the proton mass.

334 The expansion of the plasma cloud resembles the  
 335 hemispherical shock front as for a dipole obstacle in  
 336 the solar wind. For a spherical explosion, the plasma  
 337 pressure at the edge of an expanding plasma with radius  
 338  $r_{ex}$  will drop approximately as  $p \propto r_{ex}^{-2}$ . On the other  
 339 hand, the target is placed at  $d_0 = 15.5$  mm from the  
 340 rod axis, and  $r_{ex}/d_0 \ll 1$ . To first order in  $r_{ex}/d_0$ , the mag-  
 341 netic pressure increases locally as  $p_m \approx p_{m0}(1 + 2r_{ex}/d_0)$ ,  
 342

343 where  $p_{m0} \approx (8T)^2/2\mu_0 = 3 \times 10^7$  Pa, where  $p_{m0}$  is the  
 344 magnetic pressure at the surface of the target. Once  
 345  $p = p_m$ , the expansion of the plasma front will be sub-  
 346 stantially decelerated. The plasma density at the inter-  
 347 face with the magnetic field will start to grow due to  
 348 the incoming flow from behind, whose velocity becomes  
 349 larger than the expansion velocity. As the total momen-  
 350 tum of the plasma flow is fading away, the expansion  
 351 will eventually stop. The position  $r_s$  of the stopping  
 352 point is determined by equating the initial thermal en-  
 353 ergy  $E_{th}$  of the ablated plasma to the magnetic energy  
 354 in the hemispherical diamagnetic cavity. Denote the  
 355 average magnetic field by  $B$ . Then  $E_{th} = E_{mag} = V_s B^2 /$   
 356  $2\mu_0$ . The volume of the cavity is  $V_s = (2\pi/3)r_s^3$ . The en-  
 357 ergy of the laser plasma is estimated using a laser  
 358 absorption efficiency of about 70% typical for the inten-  
 359 sity used (Key et al., 1983), and subtracting the ioniza-  
 360 tion energy. The corresponding numerical values are  
 361  $E_{th} \approx 0.7 \times 4 - 0.3$  J  $\approx 2.5$  J. Averaging magnetic field  
 362 strength over the cavity volume, gives  $B \sim 9$  T. This  
 363 leads to  $\langle p_m \rangle \approx 3.2 \times 10^7$  J/m<sup>3</sup>. The resulting stopping ra-  
 364 dius is  $r_s \approx 3.3$  mm.

365 In Fig. 3, the position of the peak density gradient in  
 366 the plasma shell is plotted as function of time. The shell  
 367 appears to propagate with practically constant velocity  
 368 during the observation time, which means that a  
 369 dynamic balance is established between the magnetic  
 370 pressure and the total plasma pressure:  $\sum_{\alpha} n_{\alpha} k T_{\alpha} +$   
 371  $\rho v_0^2 = B^2 / 2\mu_0$ . Here,  $n_{\alpha}$  and  $T_{\alpha}$  are the number density  
 372 and temperature of species  $\alpha$ , in the plasma shell, respec-  
 373 tively,  $\rho$  is the mass density of the plasma,  $v_0$  the velocity  
 374 of directed motion,  $\mu_0$  the permeability of free space,  
 375 and  $k$  the Boltzmann constant. The species considered  
 376 in the summation over  $\alpha$  are electrons, protons and car-

377 bon ions. The average propagation speed of the plasma-  
 378 field interface is  $v_0 \approx 2 \times 10^5$  m/s, which is to be com-  
 379 pared to  $\sim 4 \times 10^5$  m/s, the free expansion speed deter-  
 380 mined from interferometry.

381 From interferometry, the peak plasma density in the  
 382 plasma shell is  $n_e \approx 7 \times 10^{23}$  m<sup>-3</sup>, and the plasma flow  
 383 density is  $\approx 2 \times 10^{23}$  m<sup>-3</sup>. We assume a plasma composi-  
 384 tion identical with that of the target, C:H = 1:2, and  
 385 fully ionized hydrogen and carbon at least 4 times ion-  
 386 ized. With these values we can estimate the ion density  
 387 in the plasma shell  $n_H + n_C \approx 2 \times 10^{23}$  m<sup>-3</sup> and the mass  
 388 density of the plasma flow  $\rho_H + \rho_C \approx 6 \times 10^{-4}$  kg/m<sup>-3</sup>.  
 389 The vacuum value of the magnetic field at the location  
 390 of the shell is  $B \approx 9$  T. With these values, the dynamic  
 391 balance holds for a plasma temperature  $T_e \approx 50$  eV.  
 392 The shell at the interface between the plasma and the  
 393 magnetic field is formed by the cumulation of plasma  
 394 as it interacts with the magnetic field. The steady speed  
 395 of the shell observed is attributed to be due to the  
 396 presence of a dynamic balance condition. The speed  
 397 of sound for an isothermal hydrogen plasma is  
 398  $c_s = \sqrt{(\gamma_e + \gamma_i)T/m_p} \approx 10^5$  m/s, and lower for a hydro-  
 399 gen-carbon plasma. The flow of plasma wind is super-  
 400 sonic with a Mach number  $M_s \geq 2$ .

401 We now return to the assumption regarding the ion-  
 402 ization stage of the plasma components. At 50 eV, from  
 403 a corona model of the plasma, the carbon is 4 times ion-  
 404 ized (the ionization energy for C<sup>3+</sup> to C<sup>4+</sup> is 64 eV). On  
 405 the other hand, the plasma temperature reaches much  
 406 higher values during the heating laser pulse, before it  
 407 starts the free expansion phase. According to a hydrody-  
 408 namic simulation, with MULTI (Ramis et al., 1988), the  
 409 peak plasma temperature reaches 1 keV for the condi-  
 410 tions of this experiment. The ionization energy of C<sup>5+</sup>  
 411 is about 490 eV, therefore in this early stage the carbon  
 412 is nearly fully ionized. As the plasma expands, its tem-  
 413 perature and density decrease, but the recombination  
 414 rate is too low to reduce the population of C<sup>6+</sup> by more  
 415 than a few percents for the duration of this experiment  
 416 (Kacenjjar et al., 1986).

417 The mean free path for electron-ion collisions is  
 418  $\lambda_{ei} < 50$   $\mu$ m, and is smaller than the density gradient-size  
 419 scale  $L_n \approx 0.3$ – $0.5$  mm. On the other hand, the collision  
 420 frequency is smaller or comparable with the electron  
 421 cyclotron frequency, therefore the plasma shell is mildly  
 422 collisional. For the set of plasma parameters deter-  
 423 mined, the Spitzer resistivity is  $\eta > 3 \times 10^{-6}$   $\Omega$  m so that  
 424 the magnetic field diffusion time is  $\tau_d < 40$  ns, on the  
 425 time scale of the experiment. The magnetic Reynolds  
 426 number is  $R_M < 30$ , which indicates that magnetic field  
 427 diffusion is important at this stage of the plasma dynam-  
 428 ics. This is consistent with the plasma shell propagation  
 429 beyond the stagnation point predicted by an ideal MHD  
 430 simulation.

431 In this experiment, since the ion gyroperiod is compa-  
 432 rable with the duration of the experiment, the ions are

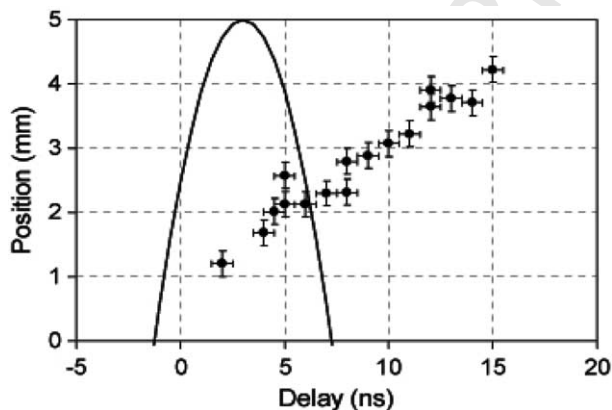


Fig. 3. The position of the peak density gradient in the plasma shell as function of time after the beginning of the heating laser pulse. It represents the result of many runs. Typically each run consists of two points separated by 7 ns. There are also a few single-shot points. The slope gives  $v_{peak} \sim 2 \times 10^5$  m/s compared to the free expansion speed which doubles this slope, and to the sonic speed:  $c_s \sim 1$  m/s which leads to a Mach number  $M_s \geq 2$ . The solid curve is the approximate representation of the laser pulse.

not magnetized. On the other hand, the electrons are magnetized at the plasma front. Indeed, for  $T_e \approx 50$  eV,  $n_e \approx 7 \times 10^{17} \text{ cm}^{-3}$ , and  $B = 10$  T, the electron gyrofrequency  $\Omega_e \approx 1.8 \times 10^{12}$  rad/s is larger than the collision frequencies with protons  $\nu_{eH} \approx 6 \times 10^{10}$  Hz and with carbon ions  $\nu_{eC} \approx 3 \times 10^{11}$  Hz. During the expansion in vacuum, this creates charge separation and a sheath potential well.

Since the magnetic field at the plasma–field interface was not measured, we do not know to what extent the magnetic field was compressed. Based on the existing experimental data, we cannot rule out the possibility that the dissipative or turbulent effects may significantly reduce the magnetic field compression at the interface.

Other parameters unchanged, the collisionless regime can be accessed with hotter plasma produced by lasers with higher energy and higher power ( $I > 10^{14} \text{ W/cm}^2$ ). Increasing the plasma temperature, the collision mean free paths can be made much longer than the plasma size and the Larmor radius. In addition, at higher initial temperature the species separation is more effective and the hydrogen-rich front can persist longer. To produce magnetized collisionless shocks, additional coils must be added to magnetize the plasma flow.

We conclude this section with a brief discussion. In this experiment, the magnetic obstacles used is generated by a current carrying rod. In the interface between laser-plasma plume and the strong magnetic field, a plasma shell is observed. The shell travels at about half the free expansion speed which suggests that the shell is formed by the cumulation of plasma at the shell interface.

The azimuthal magnetic field experiment has a positive gradient in the direction of the plasma flow and the lines are curved, with the radius of curvature of the magnetic field pointing towards the flow source. These characteristics are similar to the dipolar field commonly found in Geo-space and Astro-space bow shocks. If the parameters of the plasma flow and field are properly scaled to those of the simulated system they are thought to be relevant to the understanding of the formation of bow shocks and electron acceleration mechanisms on the day-side. Astrophysical bow shocks occur over a wide range of collisionality and ionization.

The difference in the system is that the magnetic field lines are circular instead of closing through the poles. So the plasma flow in the current experiment cannot create an auroral plasma. The plasma flow in the current experiment creates a wake that is different from that of the planetary magnetotail. Removing these difficulties is beyond the purpose of this experiment. Nevertheless, the next stage of the experiment will use a 2D dipolar magnetic field configuration attempting to reach more realistic conditions. The 2D dipolar experiment is mentioned in Horton and Chiu (2004).

The present experiment represents a first step towards the laboratory investigation of collisionless shocks. As

determined in the experiment, the plasma is collisional and the plasma flow is not magnetized except for the weak ( $B_{\text{earth}} \sim 0.3$  G) magnetic field in the laboratory. Upgrades considered for a follow-up experiment include the use of a higher intensity laser for producing a collisionless plasma, as well as means for applying a stronger ambient magnetic field. The latter is important since magnetization of the plasma flow appears to be essential for the formation of numerous SLAMS within a collisionless bow shock.

In the following section, we will see that there are two basic ingredients, which lead to an effective acceleration of electrons. They are the presence of a collisionless shock front with substantial jump in the magnetic field and the presence of high speed electrons in the plasma wind. Our next step experiment will contain both of these ingredients. Its outcome may provide insights on the electron acceleration mechanism.

### 3. Electron acceleration mechanisms

We proceed to analyze the electron acceleration in oblique shocks based on our recent investigation (Chiu et al., in press). For studies on the acceleration of ions similar to the present framework, see Usami et al. (2001), Usami and Ohsawa (2002, 2004). We will consider the interaction between quasi-normal shocks where  $B_x = B \cos \theta \ll B$ , and the high  $\beta$ -plasma where the electron speed is relatively high compared to the solar-wind speed. We have found that when the magnetic field in the shock front rises sufficiently rapidly, the gyrating trajectory of the electron can linger in the reflection region over many cycles. This leads to a large energy gain. Also, we will see there is a persistent transfer of the transverse kinetic energy into the longitudinal kinetic energy. The final energy of the accelerated electron is dominated by the parallel kinetic energy.

#### 3.1. Lorentz force on electron acceleration and the Mlm scaling solution

The motion of an electron is governed by the Lorentz force equation

$$m \frac{d\mathbf{v}}{dt} = -e(\mathbf{E} + \mathbf{v} \times \mathbf{B}). \quad (8)$$

We work with the dimensionless spatial and time variables, with the length scaled by the ion collisionless skin depth  $c/\omega_{\text{pi}}$ , and the time scaled by the inverse of the ion gyrofrequency, i.e.,  $x = c\xi/\omega_{\text{pi}}$  and  $t = \tau/\omega_c$ . Here,  $\omega_{\text{pi}} = (n_0 e^2 / \epsilon_0 M)^{1/2}$  and  $\omega_c \equiv \omega_{\text{ci}} = eB_0 / M$ . The plasma density  $n_0$  and the magnetic field  $B_0$  are defined in front of the shock. Proton is used for the ion.  $M$  is the proton mass. The velocity variable is scaled by the Alfvén speed:  $v_A = (c/\omega_{\text{pi}})\omega_c = B_0 / \sqrt{\mu_0 n_0 M}$ .

539 The dimensionless fields are defined by  $\mathbf{b} = \mathbf{B}/B_0$  and  
 540  $\mathbf{e} = \mathbf{E}/(v_A B_0)$ , with  $\mathbf{b} = (b_{x0}, 0, b_z)$  and  $\mathbf{e} = (e_x, e_y, 0)$ .  
 541 Assuming one-dimensional approximation  $b_z = b_z(x)$   
 542 and  $e_x = e_x(x)$ . Since  $\nabla \cdot \mathbf{B} = 0$ , it implies  $\partial_x B_x = 0$ , so  
 543 the  $x$ -component of the magnetic field remains to be  
 544 the same before and after the shock, or  $b_{x1} = b_{x0}$ .  
 545 (Throughout this work we will use the convention, the  
 546 script “0” is used for quantities in front of the shock,  
 547 and “1” behind the shock.) By definition,  $b_0 = 1$ , then  
 548  $b_{x0} = \cos\theta$ . The magnetic field  $b_z$  is assumed to have  
 549 the form of the damped soliton solution, which is  
 550 approximately given by

$$552 \quad b_z(\xi) = 1 + \frac{b_1 - 1}{2} \left[ 1 - \tanh\left(\frac{\xi}{d}\right) \right]. \quad (9)$$

553 Here, the thickness of the transition layer is  $2d$ . In the  
 554 quasi-normal approximation,  $b_{z1} \approx b_1$ , so the jump of  
 555  $b_z$  is  $\sim(b_1 - 1)$ . In the context of the soliton solution,  
 556 the corresponding dimensionless electric field is

$$559 \quad e_x = -\frac{db_z}{d\xi} = \frac{b_1}{2d} \cosh^2\left(\frac{\xi}{d}\right). \quad (10)$$

560 The gyroradius, the kinetic energy and the potential en-  
 561 ergy difference over a range  $\Delta y$  are given by, respec-  
 562 tively, as follows:

$$565 \quad r_e = \frac{v_\perp}{\omega_{ce}} = \frac{u_\perp v_A}{\frac{M}{m} b \omega_c} \equiv \rho_e \left[ \frac{c}{\omega_{pi}} \right] \quad \text{with } \rho_e = \frac{m u_\perp}{M b}, \quad (11)$$

$$567 \quad k_e = \frac{1}{2} m v^2 = \frac{1}{2} u^2 v_A^2 \equiv k_e [m c^2 \beta_A^2] \quad \text{with } k_e = \frac{u^2}{2}, \quad (12)$$

$$568 \quad W_e = q E_y \Delta y = q (e_{y0} v_A B_0) \left( \Delta \xi_y \frac{c}{\omega_{pi}} \right) \\
 570 \quad = \frac{M}{m} e_{y0} \Delta \xi_y \left[ \frac{m}{M} \cdot \frac{q v_A B_0 c}{\omega_{pi}} \right] \equiv w_e [m c^2 \beta_A^2] \\
 \text{with } w_e = (M/m) e_{y0} \Delta \xi_y. \quad (13)$$

571 The quantities  $\rho_e$ ,  $k_e$  and  $w_e$  are dimensionless quantities  
 572 of the electron. Those in the square brackets are units.  
 573 In terms of the Cartesian components, the dimensionless  
 574 Lorentz equation is given by

$$577 \quad \begin{pmatrix} du_x/d\tau \\ du_y/d\tau \\ du_z/d\tau \end{pmatrix} = \begin{pmatrix} -e_x \frac{M}{m} - u_y \Omega_z \\ -e_y \frac{M}{m} - u_z \Omega_x + u_x \Omega_z \\ u_y \Omega_x \end{pmatrix}. \quad (14)$$

578 Here,  $u_i = v_i/v_A$  which is the  $i$ th component of the dimen-  
 579 sionless velocity, where  $\Omega_i = M b_i/m$  is the electron gyro-  
 580 frequencies, and  $m$  the electron mass.

581 Based on Eq. (14), one may scale the time by a new  
 582 variable  $\tau^* = \tau \cdot M/m$ . This would then lead to a  $M/m$ -  
 583 scale invariant theory, except for the length parameter  
 584  $d$  in the shock structure of the fields, which breaks the  
 585  $M/m$  scale invariance in the following way. Let us fix

$M$ , increasing  $m$ , so the ratio is decreasing. Here, the  
 586 electron momentum is increasing. In turn, the electron  
 587 gyroradius  $\rho_e = m u_\perp / M b$  is increasing. Although the pre-  
 588 diction on the “energy multiplication factor” (or the  
 589 “gain factor”), depends on the  $M/m$ -scale breaking  
 590 parameter  $d/\rho$ , it turns out when  $d/\rho \ll 1$ , this factor  
 591 quickly approaches a limiting value. For the present  
 592 work, this occurs when the ration  $M/m$  is small com-  
 593 pared to the physical value:  $M/m = 1800$ .  
 594

595 Our investigation involves both numerical and ana-  
 596 lytical work. For numerical calculations, we use follow-  
 597 ing shock parameters based on the event in the SLAMS  
 598 data reported in Stasiewicz et al. (2003). The relative  
 599 velocity between the plasma and the shock is taken to  
 600 be  $v_{0x}^{\text{pl}} = -210 \text{ km/s} = -7v_A$  ( $v_A = 30 \text{ km/s}$ ). The proton  
 601 sound speed is  $c_s = 70 \text{ km/s}$  which implies that the  
 602 proton temperature is  $T_p = M c^2 \beta_s^2 = 50 \text{ eV}$ . Assuming  
 603 electron temperature is comparable to that of the  
 604 proton, the electron thermal speed in the plasma is  
 605  $v_e = \sqrt{2M/mc_s} \approx 140v_A$ . This gives  $\beta = n_0 T_e /$   
 606  $(B_0^2 / 2\mu_0) \sim 11$ , which indicates that it is indeed a high  
 607  $\beta$ -plasma. We assume the electron velocity is isotropic  
 608 in the rest frame of the plasma. Among those isotropic  
 609 points on the fixed energy shell, for the time being we  
 610 will consider the forward going electron, with its speed  
 611 relative the shock  $v_{0x} \equiv u_{0x} v_A = -147v_A$ . At the shock  
 612 front, the rise of the SLAMS event is about 100 km,  
 613 or the dimensionless half width  $d = 50 \text{ km}/$   
 614  $150 \text{ km} \sim 0.3$ . Below we will discuss two cases, the  
 615 “physical case”, where  $M/m = 1800$ , and the “ $M/m$ -scal-  
 616 ing limit case”, which is essentially the “step function”  
 617 case, for which we will take  $M/m = 20$ .

618 Fig. 4 illustrates the projection of electron trajectory  
 619 in the  $x$ - $y$  plane for the physical case where  $M/$   
 620  $m = 1800$  and  $d = 0.3c/\omega_{pi}$ . To give some background  
 621 on the shape of the trajectory shown, we find it is  
 622 instructive to first describe a simpler shape, i.e., for the  
 623  $M/m = 20$  case, where the trajectory consists of essen-  
 624 tially three sides of a rectangle. The trajectory begins  
 625 with the left-going drift. This corresponds to the first  
 626 side of the rectangle. When the gyrating-orbit first  
 627 touches the  $x = 0$  line, there is a clockwise  $90^\circ$  turn in  
 628 the drift, which leads to the upward drift. The upward  
 629 drift is accompanied by a gradual shift in the  $x$ -direc-  
 630 tion. First there is the slowing down of the shift to the  
 631 left. At around the midway of the  $y$ -drift, the  $x$ -shift  
 632 to the left slows down to stop and then turns around be-  
 633 gins shifting to the right with an increasing speed, slowly  
 634 but steadily. In this manner, the trajectory continues  
 635 drifting upward for some distance while it is persistently  
 636 shifting to the right. This upward drift constitutes the  
 637 second side of the rectangle. As the gyrating orbit leaves  
 638 the  $x = 0$  line, there is another  $90^\circ$  clockwise rotation.  
 639 Here, the  $x$ -shift reaches its final right-shifting speed,  
 640 it becomes the main drift moving to the right, which is  
 641 the third side of the rectangle.

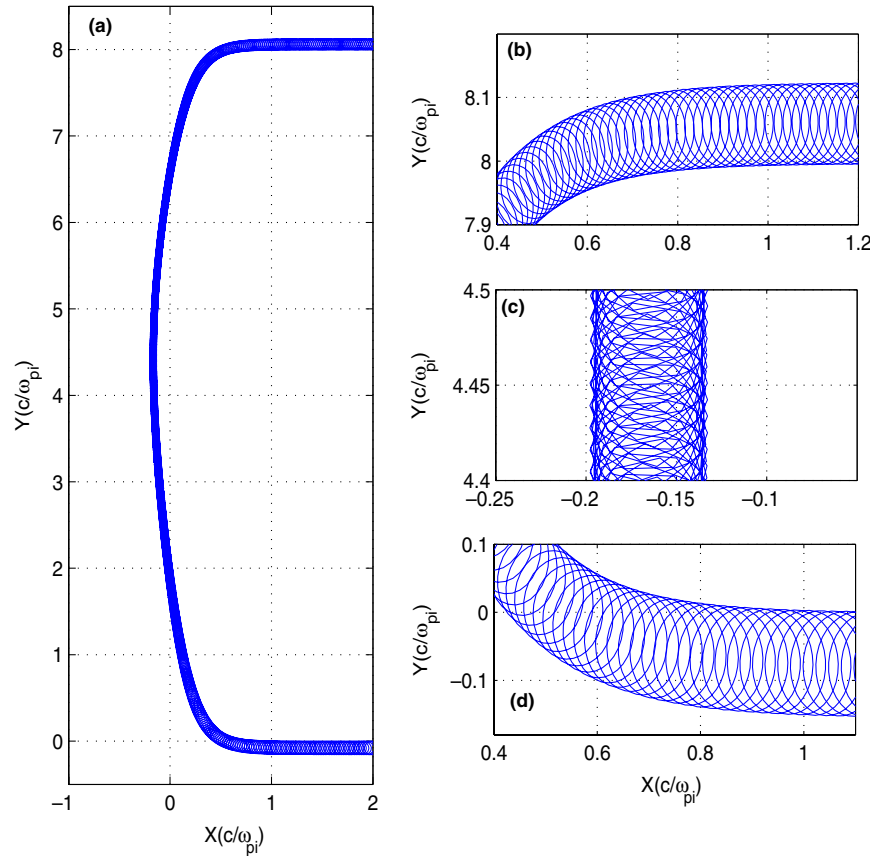


Fig. 4. The  $M/m = 1800$  case. (a) Projected trajectory in the  $x$ - $y$  plane of the gyrating electron, which is from the collision of a high- $\beta$  plasma with a shocklet near  $x = 0$ . The shock parameters are based on the reported event in the SLAMS data:  $B_{max}/B_0 = 6$ ,  $D = 50 \text{ km} \sim 0.3c/\omega_{pi}$ , except for the oblique angle. Here the quasi-normal angle is  $\theta = 88.3^\circ$ . Zoom-in views of local regions: (b) after the transient region at the exit of the  $y$ -drift (c) at the midway in the  $y$ -drift region, and (d) before the transient region at the start of the  $y$ -drift.

642 The trajectory shape for the  $M/m = 1800$  case is sim-  
 643 ilar to the scaling limit case just described except that the  
 644 two sharp  $90^\circ$  corners are replaced by the round corners  
 645 and the transition regions at both the entrance side and  
 646 exit side crudely characterized by the interval  
 647  $0 < x < 0.3c/\omega_{pi} = d$ , where  $d$  is the thickness parameter  
 648 of the shock, see Eq. (10). The  $x$ -range here is several  
 649 electron gyroradii. Notice that based on Eq. (11), in  
 650 the ambient magnetic field region, the electron gyroradi-  
 651 us is given by  $\rho_0 = mu/Mb \approx 140/1800 \sim 0.08c/\omega_{pi}$ .  
 652 See plot-a of Fig. 4. The zoom-in views: before the en-  
 653 trance transition region, at the midway and after the exit  
 654 transition region are shown, respectively, in plot-d, plot-  
 655 c and plot-b. From inspection on midway plot (plot-c)  
 656 and the overview plot (plot-a), notice that the  $x$ -coordi-  
 657 nate of the gyrating-orbits always satisfies  $x > -d =$   
 658  $-0.3$ . In other words, during the entire course of the  
 659  $y$ -drift, the electron never left the ramp. It turns out  
 660 by fine-tuning the oblique angle, the maximum stretch  
 661 in the  $y$ -drift and in turn the maximum energy gain  
 662 can be determined. The oblique angle, the  $y$ -range and  
 663 the gain factor obtained for  $M/m = 1800$  case are  
 664  $\theta = 88.3^\circ$ ,  $\Delta\xi_y = 8.2$  and  $G = 9.4$ , respectively. And for

the  $M/m = 20$  case, they are  $\theta = 88.7^\circ$ ,  $\Delta\xi_y = 1410$  and  
 $G = 19.5$ . The time evolutions of the total kinetic energy  
 (heavy-solid curve) and its parallel component (light-so-  
 lid curve) and perpendicular component (densely dotted  
 curve) for the  $M/m = 1800$  case are shown in Fig. 5(a).  
 Notice there is a persistent increase in the parallel com-  
 ponent kinetic energy and the final energy is dominated  
 by this component. Fig. 5(b) is the zoom-in view for a  
 typical small-time interval:  $[5.0, 5.1]\omega_c^{-1}$  showing that  
 there is a steady increase of  $K_{||}$  within this minute-time  
 interval. The corresponding time evolution of the energy  
 content for the  $M/m = 20$  case is shown in plot-c. Again  
 there is the steady increase and the eventual dominance  
 of the parallel component. We will come back to discuss  
 plots c-h in Section 3.3.

The gyroradius of the  $M/m = 20$  case is 90 times  
 greater than that of the  $M/m = 1800$  case. For the  $M/$   
 $m = 20$  case, the condition  $d/\rho \ll 1$  is well satisfied.  
 The  $M/m = 20$  case has essentially approached the  $M/$   
 $m$  scaling limit, i.e., the step function model. We will  
 proceed with the analytic work based on the step func-  
 tion model. We will show that the step function model  
 leads to satisfactory agreement on the  $y$ -range and gain

665  
 666  
 667  
 668  
 669  
 670  
 671  
 672  
 673  
 674  
 675  
 676  
 677  
 678  
 679  
 680  
 681  
 682  
 683  
 684  
 685  
 686  
 687

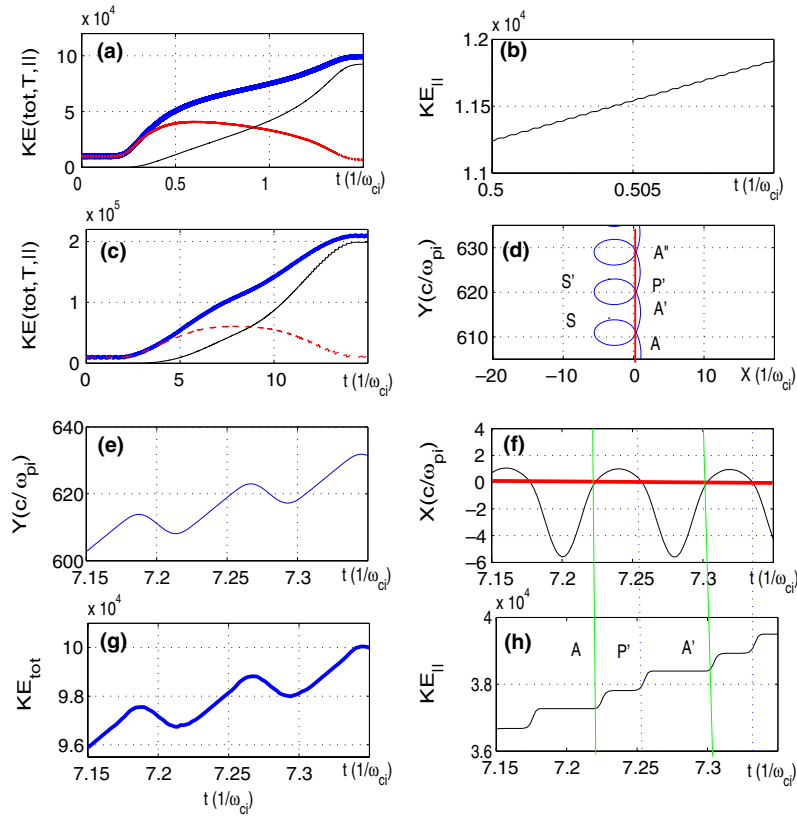


Fig. 5. The  $M/m = 1800$  case: (a) Time dependence of the total (heavy-solid), transverse (densely dotted) and parallel (light-solid) kinetic energies. Here energy is in units of  $0.005$  eV. The total energy is increased from  $50$  to  $500$  eV. (b) Zoom-in view of parallel kinetic energy at time  $t = 0.50$ – $0.51$   $1/\omega_c$ . The  $M/m = 20$  case: (c) Time dependence of total (heavy solid), transverse (dashed) and parallel (light-solid) kinetic energies. Here total energy is increased from  $50$  eV to  $\sim 1$  keV. (d) Zoom-in view of the projected trajectory in  $x$ – $y$  plane. The starting point S, and the subsequent four crossings across the  $x = 0$  line at A, P', A', P'' are indicated by the bullets. (e) The  $y$  time curve, (f) the  $x$ -time-curve with the zero crossing points A, P', A' and P'' indicated by straight lines. (g) Total energy time curve, (h) the parallel kinetic energy time curve with the staircase pattern. Notice that each step begins near the crossing across the  $x = 0$  line, see A, P', A' and P'' indicated by straight lines.

688 factor for the  $M/m = 20$  case, and gives a qualitative  
 689 understanding of these numbers for the  $M/m = 1800$   
 690 case.

### 691 3.2. Average acceleration in the shock normal-direction 692 and the total energy gain

693 With the goal of deriving a parametric form for the  
 694 energy multiplication factor, we first work on the aver-  
 695 age acceleration in the  $x$ -direction. The Lorentz force  
 696 equation Eq. (14), neglecting  $e_x$ -term, which is justified  
 697 for the high- $\beta$  case we are considering, leads to

$$699 \frac{d^2 u_y}{d\tau^2} \approx -u_y \Omega_y^2 \quad \text{or} \quad u_y = u_{\perp} \cos(\Omega_y \tau - \phi), \quad (15)$$

700 where  $\Omega_y^2 \equiv \Omega_{x0}^2 + \Omega_z^2$ . Consider the situation of a typical  
 701 gyrocycle depicted in Fig. 6 along the path: PDAB'P'.  
 702 Along PDA, which is to the left of the  $x = 0$  line, we de-  
 703 note  $u_y$  by  $u_y^L$ . Here  $\Omega_y \approx \Omega_1 = (M/m)b_1$ . Along AB'P', de-  
 704 note  $u_y$  by  $u_y^R$ , where  $\Omega_y \approx \Omega_0 \approx (M/m)[1 + (\cot \theta_0)^2/2]$ .  
 705 The average  $x$ -acceleration per cycle is given by (see Chiu  
 706 et al., in press)

$$707 \langle a_x \rangle = -\langle \Omega_{z1} u_y^L \rangle_{\text{PDA}} - \langle \Omega_{z0} u_y^R \rangle_{\text{AB'P'}} \\ \approx (\cot \theta)^2 \frac{u_{\perp}}{T} f(\phi),$$

$$709 \text{ where } f(\phi) = \sin \phi - \phi \cos \phi. \quad (16)$$

710 Notice that the averaged acceleration is a function of  $\phi$ .  
 711 In the  $y$ -drift region,  $\phi$  varies from  $\pi$  to some smaller po-  
 712 sitive angle then back to  $\pi$ . To describe the  $x$ -shift in  
 713 terms of some effective acceleration, we have made fol-  
 714 lowing simplifying assumptions. The effect of  $f(\phi)$  con-  
 715 tribution is presented by:  $\bar{f} = f(\phi_{\text{eff}})$ . We have  
 716 assigned a typical period  $T = T_1$  for gyrocycles, and typi-  
 717 cal speeds:  $\bar{u}_{\perp}$ , for the tangential speed along the path of  
 718 gyration, and  $\bar{u}_y$ , for the  $y$ -drift motion. From their def-  
 719 initions,  $\bar{u}_{\perp}/\bar{u}_y \equiv \rho_0 \Omega_0 (2\rho_0/T_1) = [M/(2m)]T_1$ . Based on  
 720 Eq. (16), the effective cycle-averaged acceleration  
 721 becomes

$$722 \langle a_x \rangle_{\text{eff}} = \frac{(\cot \theta)^2}{T_1} \cdot \left( \frac{M}{2m} T_1 \bar{u}_y \right) \bar{f} = (\cot \theta)^2 \bar{f} \bar{u}_y \cdot \frac{M}{2m}. \quad (17) \\ 724$$

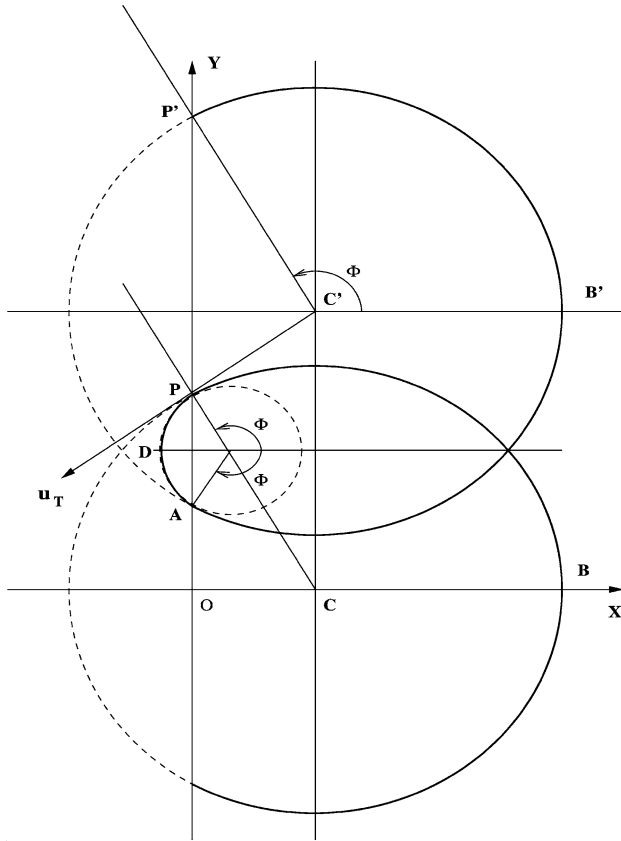


Fig. 6. Typical electron gyration orbits in an analytic model, applicable when electron gyroradius  $r_e \ll d\omega_{pi}$ . The electron follows the path: BPAB'P' with a counterclockwise gyration.

725 Following picture associated with the cycle averaged  
 726  $x$ -shift motion emerges. Before the  $y$ -drift, the gyrocenter  
 727 has the initial velocity of the plasma, so the initial  $x$ -  
 728 shift velocity is  $-u_{0x}^{pl}$ . During the  $y$ -drift, the  $x$ -shift  
 729 is governed by the effective acceleration given here. Along  
 730 the  $x$ -direction, it slows down, turns around and causes  
 731 the acceleration of the  $x$ -shift motion in the positive  $x$ -  
 732 direction. Inspection on the motion in Fig. 6 reveals that  
 733 within each gyrocycle, to the extent that one ignores the  
 734 slight change of transverse kinetic energy along the left-  
 735 hand side arc where the gyroradius is small, there is an  
 736 elastic bounce at each cycle. In turn taking  $y$ -drift as a  
 737 whole, there is an approximate overall elastic bounce  
 738 in the  $x$ -direction, i.e., at the exit end of the  $y$ -drift,  
 739 the  $x$ -shift velocity is  $\sim u_{0x}^{pl}$ . Using Eqs. (16) and (17)  
 740 the total  $y$ -drift range is given by

$$\Delta \xi_y = \frac{\bar{u}_y \cdot 2u_{0x}^{pl}}{\langle a_x \rangle_{\text{eff}}} = \frac{4}{\bar{f}} \cdot \frac{m}{M} \cdot \frac{u_{0x}^{pl}}{(\cot \theta)^2}. \quad (18)$$

744 Based on Eq. (13), which can be deduced from the Lor-  
 745 entz force equation if the  $e_x$ -term is to be neglected, Eq.  
 746 (14), the total energy increase is given by

$$K_f = K_0 \approx \left(\frac{M}{m}\right) e_{y0} \Delta \xi_y. \quad (19)$$

Using Eqs. (18) and (19), the energy multiplication factor is becomes

$$G_e \equiv \frac{K_f}{K_0} = 1 + \frac{M}{m} \frac{e_y \Delta \xi_y}{(u_0^2/2)} = 1 + \frac{8}{\bar{f}} \left( \frac{u_{0x}^{pl}}{\cot \theta u_0^2} \right)^2 \sim 1 + 4 \left( \frac{u_{0x}^{pl}}{\cot \theta u_0} \right)^2. \quad (20)$$

In the last step we set  $\bar{f} \sim 2$ , which is the scaling limit value determined based on several simulations in the parameter ranges  $2 \leq b_1 \leq 7$  and  $0.001 \leq d \leq 5$ . The value  $\bar{f}$  here turned out to be the arithmetic mean of  $f(\pi) = \pi$  and  $f(\pi/2)$ . It is gratifying that  $\bar{f}$  obtained is within the expected range.

Here is the comparison of the parametric forms of the scaling-limit given in Eqs. (18) and (20) and our simulation results. For  $M/m = 20$  case, the scaling limit prediction vs simulation results for the  $y$ -range is: (1400 vs. 1410) and for the gain is (19.2 vs. 19.5). The agreement here is within 2%. For the  $M/m = 1800$  case, for the range it is (8.8 vs. 8.2) and for the gain it is (11.0 vs. 9.4). The agreement is within 20%. To sum up, the scaling parametric form derived from the step function model, works satisfactory for the  $M/m = 20$  case and for the  $M/m = 1800$  case, it gives qualitative estimates on the range and the corresponding gain factor.

### 3.3. The temporal evolution of the total, the parallel and the transverse kinetic energies

Now, we turn our attention to the time evolution of the total, transverse and the parallel kinetic energy. Again, we will use the step-function model for our analysis below and use simulation results of the  $M/m = 20$  case as illustrated in plots c-h in Fig. 6 to verify theoretical expectations based on the analytic work.

First consider the time curve of the total energy. From Eq. (19), the profile of the total kinetic energy in time should be the same as the corresponding profile of  $y$ , which is confirmed by comparing the plot-g with the plot-e.

Away from the shock layer near  $x = 0$ , from the Lorentz force equation it can be shown that the parallel component equation of motion can be written as

$$\frac{du_{\parallel}}{d\tau} = \frac{d}{d\tau} (u_x \cos \theta + u_z \sin \theta) = -e_x \frac{M}{m} \cos \theta \approx 0. \quad (21)$$

The ramp region is defined as  $-d \leq x \leq d$ , where  $d = 0.3$ . From inspection on the plot-f, one sees that a full width in  $x$ ,  $\Delta x = 2d$  corresponds to a time interval  $\Delta t \leq 0.01$ . Away from the ramp region, the  $K_{\parallel}$  time-curve should be flat. This leads to an overall pattern: (ramp)-(short-flat-segment)-(ramp)-(long flat segment)-(ramp)... We will see below that the heights of the adjacent steps are positive definite and comparable

799 in values. So one arrives at the pattern shown in plot-h,  
800 which may be referred to as a “mixed staircase pattern”,  
801 or in short the “staircase” pattern. From inspection on  
802 the pair of plots: the  $x$ -time-curve (plot-f) and the  $K_{\parallel}$   
803 time-curve (plot-h), one sees that as expected the begin-  
804 ning of each staircase step occurs at around the point  
805 where the trajectory crosses the  $x = 0$  line, such as the  
806 4 points: A, P', A' and P'' indicated in plots-d, f and h.

807 In Chiu et al. (in press), we have shown that the jump  
808 across the line  $x = 0$  in the parallel component of the  
809 velocity, in the quasi-normal approximation for high  
810  $u_{\perp}$  case, where a  $u_z$  term may be neglected, is given by  
811

$$812 \delta u_{\parallel} \equiv u_{\parallel}^f - u_{\parallel}^i \approx u_x (\cos \theta_f - \cos \theta_i) \\ 813 \approx | \theta_f - \theta_i | u_{\perp} \sin \phi > 0. \quad (22)$$

814 Notice that since  $\cos \theta = b_{0x}/b$ , the stronger is the local  
815 magnetic field, the smaller is  $\cos \theta$ , or the closer is  $\theta$  to  
816  $90^\circ$ . Thus as the point  $x = 0$  is crossed for both entrance  
817 and the exit cases, the product  $u_x (\cos \theta_f - \cos \theta_i)$  is  
818 always positive definite. In particular for the entrance  
819 case, sign [RHS] =  $(-)(-) = +$  and for the exit case, sign  
820 [RHS] =  $(+)(+) = +$ . So the jump associated with the  
821 crossing of the  $x = 0$  line from either side gives a positive  
822 definite quantity. Since both  $u_{\perp}$  and  $\phi$  at  $x = 0$ -crossing  
823 points are slowly varying functions of time, Eq. (22) that  
824 heights of successive jumps in  $u_{\parallel}$  are expected to vary  
825 slowly as a function of time. Plot-h confirms the features  
826 described.

827 Now, we return to plot-b, which is the  $K_{\parallel}$  time-curve  
828 for  $M/m = 1800$  case. We extend Eq. (22) in the following  
829 manner. Taking account that  $b$  is a smooth function of  $x$ ,  
830 for a typical  $i$ th differential increment  $dx = x_{i+1} - x_i$

$$832 \delta u_{\parallel} = u_x \frac{d \cos \theta}{dx} dx = u_x \left[ -\frac{b_{0x}}{b^2} \frac{db}{dx} \right] (x_f - x_i). \quad (23)$$

833 For the  $x$ -component moving along the negative  $x$ -  
834 direction, which goes upward along the ramp, the sign  
835 of the right hand side is:  $(-)[+](-) = +$ . For the  $x$ -com-  
836 ponent moving along the positive  $x$ -direction, it is corre-  
837 spondingly,  $(+)[+](+) = +$ . So within the quasi-normal  
838 approximation, for a smooth ramp instead of a step  
839 function, we expect there is a steady increase of  $u_{\parallel}$ .  
840 Plot-b confirms this trend.

841 To sum up the total kinetic energy is the sum of the  
842 transverse plus parallel kinetic energy. To the extend  
843 that we ignore the  $e_x$ -term, there is no jump in the total  
844 energy. The building up of the parallel kinetic energy  
845 across the  $x = 0$  line is supplied by the transverse  
846 momentum. Furthermore, the approximate elastic  
847 bounce picture mentioned in Section 3.2 implies that  
848 the initial and the final transverse kinetic energy should  
849 be comparable, so the increase of the total kinetic en-  
850 ergy, i.e.,  $K_f - K_i \approx (M/m)e_{y0} \Delta \zeta_y$ , of Eq. (19) should  
851 have predominantly the parallel component of the ki-  
852 netic energy.

853 In this work we assume that, in the rest frame of the  
854 solar wind plasma, the electron velocity is approxi-  
855 mately isotropic. The two cases we have considered have  
856 the initial electron moving along the  $x$ -direction. We  
857 have also studied how the energy multiplication factor  
858 varies as a function the rest frame azimuthal angle for  
859 various fixed values of the rest frame polar angles. For  
860 the  $M/m=20$  case, where the gain is  $\sim 20$ , we found that  
861 about 1/3 of electrons on the fixed energy shell of inter-  
862 est has a multiplicative factor greater than 10. One may  
863 conclude that significant fraction of the electrons on the  
864 energy shell, which are being accelerated to an energy  
865 over half of the maximum accelerated energy.

#### 866 4. Conclusions

867 An experimental simulation of planetary magneto-  
868 spheres is being developed to investigate the formation  
869 of collisionless bow shocks and the magnetospheres  
870 from magnetic (dipolar) obstacles. The plasma and solar  
871 wind are simulated by laser ablation is launched perpen-  
872 dicular to the magnetic field of a high-current discharge.  
873 The ablation plasma is created using the Tomcat laser,  
874 currently emitting 5 J in a 6 ns pulse at 1  $\mu\text{m}$  wavelength  
875 and irradiance above  $10^{13} \text{ W/cm}^2$ . The high impedance  
876 Zebra  $z$ -pinch generator, with load current up to 1 mA  
877 is used to produce the magnetic fields. Theoretical mod-  
878 eling (Horton and Chiu, 2004) is used to estimate the  
879 plasma parameters achievable at the front of the blow-  
880 off and to optimize the experimental design. Time-gated  
881 schlieren imaging and interferometry are used to detect  
882 the density space distributions. Diagnostics to be added  
883 include time-gated spectroscopy for temperature for  
884 density measurements, as well as Faraday rotation with-  
885 in the plasma and spectroscopic techniques to determine  
886 the magnetic field, all with space resolution. The results  
887 of initial experiment reported here indicate the presence  
888 of a plasma-shell at the interface between the plasma  
889 and the strong magnetic field region.

890 During the next-step proof of principle laser- $Z$ -pinch  
891 experiments with the University of Nevada–Texas col-  
892 laboration, the emphasis is on documenting the change  
893 in the magnetic geometry due to the plasma wind includ-  
894 ing the existence of the magnetic tail and the creation of  
895 the magnetopause behind a bow shock. The measure-  
896 ment of the change in the magnetic field may be carried  
897 out using the Faraday rotation instruments and mag-  
898 netic probes.

899 Motivated by the new high resolution, spatially res-  
900 olved measurements from the Four-Cluster spacecrafts  
901 of the microstructure in the Earth's bow shock, we have  
902 presented a laboratory simulation proposed for creating  
903 bow shocks from the laser blow-off plasmas and the  
904 strong ( $B \sim 10\text{--}100 \text{ T}$ ) magnetic field produced by  
905 capacitance powered exploding wires (Bauer et al.,

1997) and (Chittenden et al., 2004). The flat top time for the magnetic field exceeds  $1 \mu\text{s}$ , so that, we may have a quasistationary shock front for  $\omega_{ce}\Delta t/2\pi \sim 10^6$  cyclotron periods.

We have presented two numerical simulations which involve electron acceleration during the collision of a high- $\beta$ -plasma wind with a SLAMS-type shocklet. Our numerical work is based on the shock parameters:  $B_0 = 2 \text{ nT}$ , the half-width of the rise  $D = 50 \text{ km}$  and the mach number  $M_s = 6$ . When the physical ratio  $M/m = 1800$  was used, a 10-fold energy gain was obtained. Using  $M/m = 20$ , which is close to the scaling limit, the corresponding energy gain is about 20-fold. The latter shows that as the parameter value of  $D$  is reduced, there is a most a factor of 2 gain in energy. Of course the higher the mach number could also lead to higher energy gain. Furthermore, we envision that electrons can undergo acceleration in stages, when there are successive plasma-wind-shocklet collisions. The higher is the electron energy, the larger is its gyroradius which would lead to a longer  $y$ -drift, and in turn to a more rapid increase in its energy. Taking all these factors into account, we find an energy-gain by a factor of 50–100 or even beyond is not out of reach.

From our fixed-energy-shell ensemble study, we found there was a significant fraction of electrons on the shell which have been accelerated to over half of the maximum accelerated energy. This leads us to suggest that the local plasma near a shocklet should in general be at somewhat higher temperature. The finding of the large fluctuations in high momentum portion of the electron momentum distribution near shocklets could be significant, since large fluctuations here may be an indication of the presence of different stages of electron accelerations.

In view of the universal appearance of shocks in space and astrophysics we argue that it is important to have several independent attempts at modeling collisionless plasma shocks in the laboratory.

## 5. Uncited reference

Li (2000).

## Acknowledgements

This work is supported by NSF ATM 0229863 and DOE/NNSA under UNR grant DEFC08-01NV14050. The authors thank A.L. Astanovitskiy, B. Le Galloudec, and P.J. Laca for help with the experiments.

## References

- Bauer, B.S., Kantsyrev, V.L., Winterberg, F., Shlyaptseva, A.S., Mancini, R.C., Li, H., Oxner, A. The Dense Z-Pinch Program at the University of Nevada, Reno, in: Pereira, N.R., Davis, J., Pulsifer, P.E. (Eds.), American Institute of Physics Proceedings "Dense Z-Pinches: Fourth International Conference", vol. 409, 1997, p. 153. Available from: <<http://www.ntf.unr.edu/Z-pinch/zbib.htm>>.
- Chittenden, J.P., Lebedev, S.V., Oliver, B.V., Yu, E.P., Cuneo, M.E. Phys. Plasmas 11 (3), 1118, 2004.
- Chiu, C., Horton, W., Ohsawa, Y. Large electron acceleration by the microstructure of shocks (in press).
- Dessler, A.J. (Ed.). Physics of the Jovian Magnetosphere. Cambridge University Press, Cambridge, 1983.
- Escoubet, C.P., Laakso, H., Goldstein, M., Paschmann, G., in: Proceedings of the Conference on Earth–Sun Connection. Cluster: New Measurements of Plasma Structure in 3D, Kona, Hawaii, 2004.
- Fälthammar, C.G. Laboratory experiments of magnetospheric interest. Space Sci. Rev. 15, 803, 1973.
- Horton, W., Chiu, C. Phys. Plasmas 11, 1645, 2004.
- Kacenjar, S. et al. Phys. Fluids 29, 2007, 1986.
- Key, M.H., Toner, W.T., Goldsack, T.J., Kilkenny, J.D., Veats, S.A., Cunningham, P.F., Lewis, C.L.S. Phys. Fluids 26, 2011, 1983.
- Li, Xinlin. Modeling particle injections-test particle simulations (PDF), in: Proceedings of the Fifth International Conference on Substorms, vol. 369, ESA, 2000.
- Li, Xinlin Radiation belts and substorm particle injections (PDF). In: Winglee, R.M. (Ed.), Proceedings of the Sixth International Conference on Substorms, p. 305, 2002.
- Li, X., Baker, D.N., Temerin, M., Reeves, G., Belian, R. Simulation of dispersionless injections and drift echoes of energetic electrons associated with substorms? (PDF). Geophys. Res. Lett. 25, 3763, 1998.
- London, R.A., Rosen, M.D. Phys. Fluids 29, 3813, 1986.
- Ramis, R., Schmalz, R., Meyer-Ter-Vehn, J. Comp. Phys. Commun. 49, 475, 1988.
- Sarris, T.E., Li, X., Tsaggas, N., Paschalidis, N. Modeling energetic particle injections in dynamic pulse fields with varying propagation speeds. J. Geophys. Res. 107, 2002.
- Shapiro, S.L., Teukolsky, S.A. Black Holes, White Dwarfs and Neutron Stars. The Physics of Compact Objects. Wiley, New York, 1983.
- Stasiewicz, K., Shukla, P.K., Gustafsson, G., Buchert, S., Lavraud, B., Thidé, B., Klos, Z. Phys. Rev. Lett. 90, 085002, 2003.
- Summers, D., Thorne, R.M. J. Geophys. Res. 108 (A4), 1143, 2003.
- Summers, D., Thorne, R.M., Xiao, F. Relativistic theory of waveparticle resonant diffusion with application to electron acceleration in the magnetosphere. J. Geophys. Res. 103, 20487, 1998.
- Summers, D. et al. Geophys. Res. Lett. 29, 2174, 2002.
- Tajima, T., Shibata, K. Plasma Astrophysics. Perseus Publishing, Cambridge, MA, ISBN 0-8133-3996-0, 2002.
- Usami, S., Ohsawa, Y. Phys. Plasmas 9, 1069, 2002.
- Usami, S., Ohsawa, Y. Phys. Plasmas 11, 918, 2004.
- Usami, S., Hasegawa, H., Ohsawa, Y. Phys. Plasmas 8, 2666, 2001.
- Zel'dovich, Ya.B., Raizer, Yu.P. In: Hayes, W.D., Probstein, R.F. (Eds.), Physics of Shock Waves and High-temperature Hydrodynamics Phenomena. Academic Press, New York and London, 1966, See Chapter VII.